Magnetic properties of $HoCoC_2$, $HoNiC_2$ and their solid solutions

H. Michor[a,**], S. Steiner[a], A. Schumer[a], M. Hembara[b], V. Levytskyy[b], V. Babizhetskyy[b], B. Kotur[b]

[a] *Institute of Solid State Physics, TU Wien, Wiedner Hauptstrasse 8-10, A-1040 Wien, Austria*
[b] *Department of Inorganic Chemistry, Ivan Franko National University of Lviv, Kyryla and Mefodiya Str., 6, UA-79005 Lviv, Ukraine*

Abstract

Magnetic properties of single crystalline $HoCoC_2$ and the evolution of magnetic and structural features in a series of polycrystalline solid solutions $HoCo_{1-x}Ni_xC_2$ ($0 \leq x \leq 1$) are investigated by means of x-ray diffraction, magnetization, magnetic susceptibility and specific heat measurements. The crystal structures of all investigated samples refers to the $CeNiC_2$-type structure (space group *Amm*2 and Pearson symbol oS8). Non-isoelectronic substitution of Co by Ni causes a non-linear increase of the unit cell volume and especially a non-monotonous variation of the *a* and *c* lattice parameters as well as a pronounced reduction of the C-C bond length of carbon dimers. Temperature dependent magnetization and specific heat measurements reveal a crossover from a ferromagnetic for $HoCoC_2$ with $T_C = 10.6(1)$ K to an antiferromagnetic ground state for $HoNiC_2$ with $T_N = 2.78(6)$ K and a non-monotonous variation of the magnetic ordering temperature with a minimum at intermediate compositions. Crystalline electric field effects of $HoCoC_2$ and $HoNiC_2$ are analysed using combined thermodynamic and magnetic susceptibility data. The electrical resistivity of $HoNiC_2$ displays a distinct anomaly near room temperature which indicates the formation of a charge density wave (CDW) state as earlier reported for several other rare earth nickel dicarbides.

Keywords: Rare-earth transition metal carbides, Magnetic properties, Crystalline electric field, Charge density wave, Heat capacity

1. Introduction

Carbide intermetallics containing rare earths and 3*d* transition metals attract enduring interest with respect to their large variety of $4f$-$3d$ magnetic states as well as with respect to charge density wave phenomena, especially in $RNiC_2$ [1, 2], and unconventional superconductivity in $LaNiC_2$ [3, 4]. Respective ternary dicarbides, RTC_2 with R = rare earth and T = Fe, Co, and Ni occur in two structure types. The iron and nickel containing rare earth carbide intermetallics, $RFeC_2$ (R = Sm, Gd – Er, Lu) and $RNiC_2$ (R = La – Lu), crystallize in the non-centrosymmetric orthorhombic $CeNiC_2$-type structure, space group *Amm*2 [5, 6]. $RCoC_2$ compounds display two structure types. Those with light rare earths (R = La – Sm) adopt the monoclinic $CeCoC_2$-type structure, space group *Bb* [6, 7], while those with heavy rare-earths (R = Gd – Lu) crystallize in the orthorhombic $CeNiC_2$-type structure. Both structure types are closely related to each other, i.e., the monoclinic type can be regarded as a distorted version of the orthorhombic one. Contrary to the $RFeC_2$ carbides, those with Co and Ni are remarkably stable in air.

The magnetic structures of $RCoC_2$ and $RNiC_2$ with R = Pr, Nd, Tb – Tm have been extensively studied by powder neutron diffraction (PND). A survey of these results was compiled by Schäfer *et al.* [8]. The majority of $RCoC_2$ compounds adopt a ferromagnetic (FM) ground state at low temperatures, e.g. $HoCoC_2$ with a reported Curie temperature $T_C \simeq 9$ K [9], whereas $RNiC_2$ compounds show different types of antiferromagnetic (AFM) ground state configurations, e.g. $HoNiC_2$ adopts a two-component non-collinear AFM structure at a Néel temperature reported as $T_N \sim 4$ K [10]. In all $RCoC_2$ and $RNiC_2$ compounds magnetic order is essentially confined to the rare earth $4f$ moments while 3*d* moments remain negligible.

Our present interest lies in the crossover from FM to AFM ordering of the rare earth sublattice in quasi-ternary systems $RCo_{1-x}Ni_xC_2$ as well as in crystallographic peculiarities caused by non-isoelectronic substitution of Co by Ni. Recently, the crystal structure and evolution of magnetic properties in the solid solution series $DyCo_{1-x}Ni_xC_2$ isotypic with orthorhombic $CeNiC_2$ have been reported [11]. In this series, the substitution of Co by Ni causes a remarkable deviation of the unit cell volume from Vegard's rule and a non-monotonous variation of the *a* and *c* lattice parameters with extrema at $x \sim 0.35$. A crossover from FM to AFM ordering is accompanied with a significant reduction of the magnetic ordering temperature at intermediate compositions near $DyCo_{1/3}Ni_{2/3}C_2$. Here, we report on crystallographic characteristics and on magnetic properties of the series $HoCo_{1-x}Ni_xC_2$ ($0 \leq x \leq 1$) as well as a single crystal study of $HoCoC_2$.

**Corresponding author
Email address: michor@ifp.tuwien.ac.at (H. Michor)

2. Material and methods

2.1. Synthesis

The polycrystalline samples $HoCo_{1-x}Ni_xC_2$ with compositions x = 0, 0.25, 0.50, 0.75, 1.0 have been prepared by arc melting with subsequent homogenization at 1070 K for one month using a procedure described earlier [11]. Commercially available elements, Ho sublimed bulk pieces (Alfa Aesar, 99.9 at.%), powders of electrolytic nickel and cobalt (Strem Chemicals, purity of 99.99 at.%) and graphite powder (Aldrich, 99.98 at.%), were used. Single crystalline $HoCoC_2$ has been grown from stoichiometric polycrystalline starting material via the Czochralski technique in a tetra-arc furnace from Techno Search Corp.

2.2. Diffraction and sample characterization

Powder X-ray diffraction (XRD) patterns for full profile refinements of the series $HoCo_{1-x}Ni_xC_2$ were collected on a STOE STADI P powder diffractometer with monochromated Cu-$K_{\alpha 1}$ radiation ($10° \leq 2\Theta \leq 100°$, step size 0.05°) to check the samples homogeneity. For precise lattice parameters refinements the data were collected at room temperature on a Siemens D5000 powder diffractometer with graphite monochromated Cu-K_α radiation ($20° \leq 2\Theta \leq 120°$, step size 0.02°) a powder of germanium (99.9999%, a_{Ge} = 5.657905 Å) served as internal standard. All polycrystalline samples $HoCo_{1-x}Ni_xC_2$ were examined using energy dispersive X-ray spectroscopy analysis with a scanning electron microscope REMMA-102-02, whereby only Ho, Ni and Co concentrations were examined.

Czochralski grown, single crystalline $HoCoC_2$ was oriented by means of a standard Laue technique and cut accordingly into a set of three bar shape single crystals with their longest edges oriented parallel to the principal a, b and c axis directions, with masses of 10 to 20 mg. Another crystal was cut in approximately cubic shape with a mass near 70 mg.

2.3. Low temperature physical properties

Specific heat measurements on polycrystalline samples of about 1 g were performed by means of a home-made adiabatic step heating technique at temperatures ranging from 2 K to 140 K and in magnetic fields up to 2 T (see Ref. [12] for details of the set-up). Additional specific heat measurements based on relaxation-type technique were carried out with a Quantum Design PPMS for a $HoCoC_2$ single crystal oriented with c-axis parallel to the externally applied field (2 – 200 K and 0 to 5 T). Single crystal and polycrystal specific heat data of $HoCoC_2$ are essentially matching, just the adiabatic measurement of the polycrystalline sample provides a much higher resolution in the temperature steps. For $HoNiC_2$ additional zero-field heat capacity data down to 0.4 K were collected using a PPMS ^{3}He heat capacity insert. Temperature and field dependent magnetic measurements were carried out on a CRYOGENIC SQUID magnetometer with a temperature range from 3 K to room temperature applying static magnetic fields up to 6 T. Additional temperature dependent magnetisation measurements (3 – 400 K) as well as field dependent isothermal magnetization measurement at 2 K and fields up to 9 T were performed for $HoCoC_2$ single crystals with principal crystallographic orientations parallel to the applied field using a PPMS vibrating sample magnetometer. Temperature dependent resistivity measurements for polycrystalline $HoNiC_2$ were performed using a Quantum Design PPMS set-up in a temperature range from 2 – 360 K. All other samples of the series $HoCo_{1-x}Ni_xC_2$ including a $HoCoC_2$ single crystal (current parallel to the orthorhombic a axis) were measured in a home-made set-up in the temperature range from 4.2 K to room temperature. All resistivity measurements were conducted with a four-point ac measuring technique on bar shape samples with spot welded gold contacts.

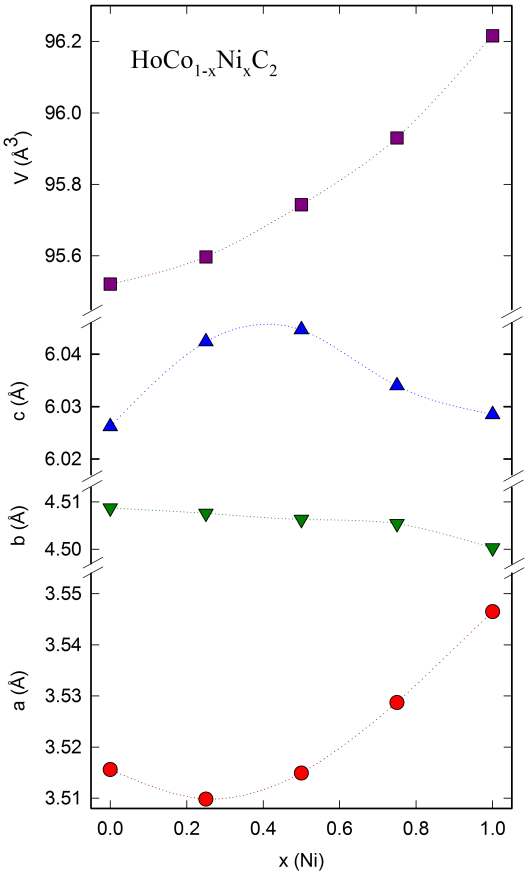

Figure 1: Variation of the lattice parameters of solid solutions $HoCo_{1-x}Ni_xC_2$ (dotted lines are guides to the eye).

3. Results and Discussion

3.1. Structural characterization

XRD data of the $HoCo_{1-x}Ni_xC_2$ series were indexed in the $CeNiC_2$ structure type, space group $Amm2$, thus, confirming a continuous solid solubility between $HoCoC_2$ and $HoNiC_2$. Refined cell parameters of the series are summarized in Table 1. The present results of $HoCoC_2$ and $HoNiC_2$ are in good agreement with earlier reported data in Ref. [6].

The unit cell parameters of pseudo-ternary series $HoCo_{1-x}Ni_xC_2$ are displayed in Fig.1. The unit cell vol-

ume increases with increasing Ni content with a negative deviation from Vegard's rule, as it was observed for the related series $DyCo_{1-x}Ni_xC_2$ [11]. Again, a non-linear variation of the a and b lattice parameters is observed which may result from the non-isoelectronic substitution of Co by Ni where one extra electron is progressively added in the series $HoCo_{1-x}Ni_xC_2$. The latter may also be responsible for a systematic reduction of the C–C bond length which is indicated by the present XRD results. The C–C inter-atomic distances of $HoCoC_2$ and $HoNiC_2$ have, of course, been determined more accurately via earlier PND studies [9, 10] yielding 1.422 Å and 1.373 Å, respectively, thus, indicating a change of the bonding character of C–C dimers by Co/Ni substitution. Reference values of single and double C–C bond lengths are e.g. 1.54 Å in diamond and 1.34 Å in alkene, respectively. This indicates some change of the electronic structure due to Co/Ni substitution in the series $HoCo_{1-x}Ni_xC_2$.

x(Ni)	lattice parameters (Å)			V (Å^3)
	a	b	c	
0.00	3.5156(1)	4.5087(1)	6.0262(1)	95.5197(3)
0.25	3.5098(2)	4.5076(2)	6.0424(2)	95.5954(6)
0.50	3.5149(1)	4.5063(2)	6.0447(2)	95.7432(5)
0.75	3.5287(2)	4.5054(2)	6.0340(2)	95.9298(6)
1.00	3.5465(1)	4.5003(2)	6.0285(1)	96.2157(4)

Table 1: Room temperature lattice parameters of solid solutions $HoCo_{1-x}Ni_xC_2$ as labeled. Structure type $CeNiC_2$, space group $Amm2$.

3.2. *Specific heat and magnetic susceptibility of the solid solution series $HoCo_{1-x}Ni_xC_2$*

The evolution of magnetic ordering temperatures in the solid solution $HoCo_{1-x}Ni_xC_2$ is revealed by the specific heat results depicted in Fig. 2. The magnetic phase transition temperatures determined from the magnetic specific heat anomalies display a non-monotonous variation from $T_C = 10.6(1)$ K for $HoCoC_2$ to $T_N = 2.78(5)$ K for $HoNiC_2$. The lowest transition temperature is observed for $HoCo_{0.25}Ni_{0.75}C_2$ with a presumably AFM Néel temperature, $T_N = 2.4(1)$ K. Accordingly, we expect a minimum of the ordering temperature somewhere on the Ni-richer side, most likely in the composition range $0.5 < x < 0.75$. We note, that the Curie temperature of $HoCoC_2$, $T_C = 10.6(1)$ K obtained from the present thermodynamic data, is markedly higher than the earlier reported value, $T_C \simeq 9$ K, evaluated from PND data [9]. For the other end of the solid solution, $HoNiC_2$, specific heat data indicate a distinctly lower phase transition temperature $T_N = 2.78(5)$ K as compared to $T_N \sim 4$ K reported from PND studies [10]. The latter value may relate to short range correlations which possibly cause the pronounced tail which appears above the distinct second order anomaly of $HoNiC_2$ in Fig. 2 (i.e. above 2.8 K). The present specific heat data of $HoNiC_2$ are in fair agreement with data reported earlier [13] where an ordering temperature of 3 K has been determined from a slightly less distinct specific heat anomaly.

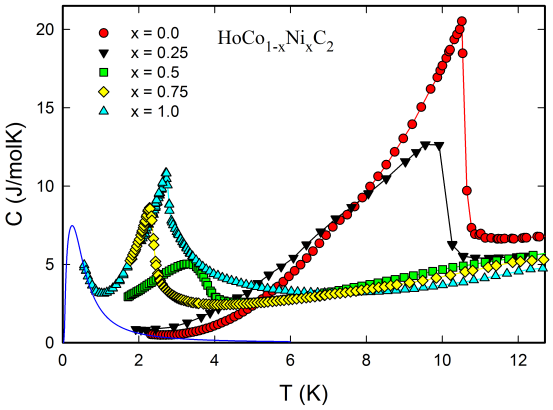

Figure 2: Temperature dependent specific heat, $C(T)$, of polycrystalline samples of solid solutions $HoCo_{1-x}Ni_xC_2$ as labeled. The solid blue line indicates a Ho nuclear Schottky contribution (see section 3.4).

The temperature dependent inverse dc magnetic susceptibilities, $H/M \equiv 1/\chi$, of single crystalline $HoCoC_2$ averaged with respect to the principal orientations and of fixed powders of polycrystalline $HoNiC_2$ and solid solutions $HoCo_{1-x}Ni_xC_2$ is displayed in Fig. 3. For the temperature interval from 30 K to room temperature, a modified Curie-Weiss model, $\chi(T) = \chi_0 + C/(T - \theta_p)$, applies well to describe the temperature dependence of the inverse susceptibility data (fits are indicated as solid lines in Fig. 3). Thereby, χ_0 stands for a temperature independent, Pauli-like component of the susceptibility, θ_p for the paramagnetic Curie-Weiss temperature, and C is the Curie constant which relates to the effective paramagnetic moment, $\mu_{\rm eff}$, by $C = N_A\mu_{\rm eff}^2/3k_B$.

Several features and trends revealed by the analysis of the $1/\chi$ data in Fig. 3 in terms of the modified Curie-Weiss model are closely following our earlier observations on the related series $DyCo_{1-x}Ni_xC_2$ [11]: The Pauli paramagnetic components χ_0 vary from about 3×10^{-3} emu/mol for $HoCoC_2$ to about 0.8×10^{-3} emu/mol for $HoNiC_2$. The effective paramagnetic moment of $HoNiC_2$, $\mu_{\rm eff} = 10.6\,\mu_B$/f.u., essentially matches the theoretical free ion value of Ho^{3+} ($10.58\,\mu_B$), and is in close agreement with a directional average of the effective moment, $\mu_{\rm eff} = 10.5\,\mu_B$/f.u., evaluated from single crystal susceptibility data of $HoNiC_2$ by Koshikawa *et al.* [14]. All cobalt containing solid solutions $HoCo_{1-x}Ni_xC_2$ and their parent compound $HoCoC_2$ exhibit slightly reduced effective paramagnetic moments ranging from 10.2 to $10.5\,\mu_B$. From orientation averaged single crystal SQUID data of $HoCoC_2$ we obtain $\mu_{\rm eff} = 10.3(1)\,\mu_B$/f.u. and using orientation averaged VSM susceptibility data of a 70 mg $HoCoC_2$ single crystal and an extended temperature interval 30 – 390 K (see section 3.5) for this fit, we obtain $\mu_{\rm eff} = 10.5(1)\,\mu_B$/f.u. and slightly lower $\chi_0 \simeq 2 \times 10^{-3}$ emu/mol For the corresponding Dy-based solid solutions a similar, but more pronounced and monotonous increase of the effective moment from $DyCoC_2$ towards $DyNiC_2$ has been reported [11]. The paramagnetic Curie-Weiss temperatures θ_p obtained for $HoCo_{1-x}Ni_xC_2$ finally reveal a sign

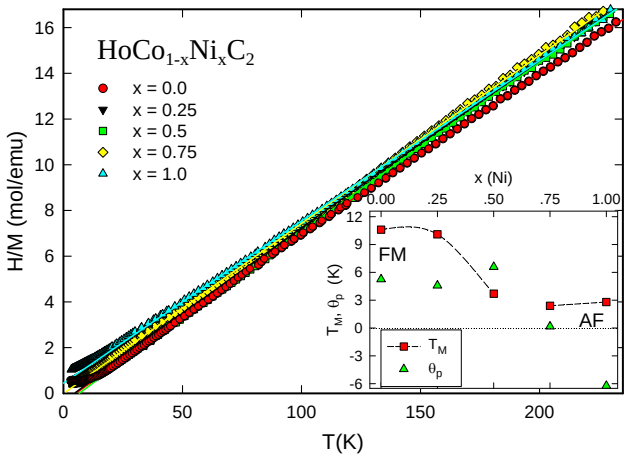

Figure 3: Temperature dependent inverse magnetic susceptibility, H/M, measured at 1 T on fixed powder samples of the series $HoCo_{1-x}Ni_xC_2$ as labeled. For $HoCoC_2$, the average of single crystal measurements in principal orientations is displayed. Solid lines are fits by a modified Curie-Weiss law (see text). Insert: magnetic phase diagram of composition dependent transition temperatures, T_M, and paramagnetic Curie temperatures, θ_p; dashed lines connecting T_M are guides to the eye.

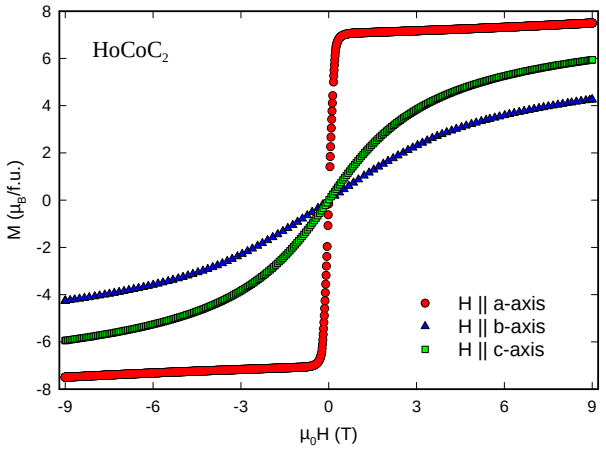

Figure 4: Isothermal, field dependent magnetization of single crystalline $HoCoC_2$ measured at 2 K for principal orientations of the magnetic field as labeled.

change (in line with the transition from a FM to an AFM ground state) which was also observed for the related Dy-based series [11]. The Co/Ni composition dependent variation of the magnetic phase transition temperatures, T_M, and the paramagnetic Curie-Weiss temperatures, θ_p, are summarized as a magnetic phase diagram depicted as insert in Fig. 3.

3.3. Single crystal study of the magnetic anisotropy of $HoCoC_2$

While details of the magnetic anisotropy of single crystalline $HoNiC_2$ have been reported earlier [14], a corresponding investigation was still pending for $HoCoC_2$. Ferromagnetism with Ho-4f spontaneously ordered magnetic moments, $\mu_{so} = 6.6(1)\,\mu_B$ (at 1.7 K), oriented in the crystallographic a axis direction has been proposed from powder neutron diffraction on $HoCoC_2$ by Schäfer *et al.* [9]. The 2 K magnetic isotherms, $M(H)$, of the present $HoCoC_2$ single crystal displayed in Fig. 4 for $H\|a$, $H\|b$, and $H\|c$ confirm the a axis as the easy direction of magnetization, but reveal a slightly larger spontaneously ordered magnetic moment, $\mu_{so} = 7.10(6)\,\mu_B$, at 2 K. Corresponding temperature dependent inverse magnetic susceptibility data, $H/M(T)$, presented for the same principal orientations in Sec. 3.5 further reveals the a axis as the easy direction of the single ion CEF anisotropy (see below).

Additional temperature and field dependent specific heat data of a $HoCoC_2$ single crystal measured with $H\|a$-axis orientation (not shown) reveal a magnetic field induced broadening and shift of the magnetic specific heat anomaly towards elevated temperatures which is well in line with the behavior of a collinear FM state.

3.4. Magnetic specific heat contribution and magnetic entropy gain

The 4f magnetic specific heat contributions of $HoCoC_2$ and $HoNiC_2$ are extracted from the total heat capacities displayed in Fig. 2 by subtracting conduction electron and lattice contributions via specific heat reference data of $LuCoC_2$ and $LuNiC_2$, respectively [15]. For the evaluation of the magnetic entropy gain, in particular for $HoNiC_2$, it is further necessary to evaluate and subtract the magnetic contributions of $^{(165)}$Ho nuclei with $I = 7/2$ nuclear spin, saturated nuclear moment $\mu_{sn} = 2.108 \times 10^{-26}$ J/T and rather large hyperfine interaction. The hyperfine splitting of the $J = 7/2$ multiplet causes a nuclear Schottky specific heat anomaly well below 1 K whose tail, however, is clearly visible as low temperature upturn of the specific heat data in Fig. 2. For elemental Ho metal nuclear specific heat contributions have been studied by Gordon *et al.* [16] and they proposed a simple Curie-type (non-interacting) paramagnetic model to account for the nuclear specific heat contribution. Accordingly, we adjust and subtract this contribution by the relation, $C_{nuc}(T) = \mathrm{R}x^2B_I'(x)$, with $x = \mu_0\mu_{sn}H/k_BT$, $B_I'(x)$ being the derivative of the Brillouin function and R the gas constant. Using $\Delta_{nuc} \equiv \mu_0\mu_{sn}H/k_B$ as a fitting parameter, we obtain $\Delta_{nuc} \simeq 0.86$ K for $HoCoC_2$ from data starting at 2.3 K and almost identical $\Delta_{nuc} \simeq 0.84$ K for $HoNiC_2$ from lower temperature data down to 0.4 K. The latter, $C_{nuc}(T)$ for $HoNiC_2$, is shown as solid line in Fig. 2. The present values for the overall splitting of the Ho nuclear multiplet are of similar magnitude as $\Delta_{nuc} \simeq 1.36$ K obtained for elemental Ho metal [16].

The temperature dependent magnetic specific heat contributions $C_{4f}(T)$ of $HoCoC_2$ and $HoNiC_2$, obtained by subtracting conduction electron, phonon, and nuclear contributions via the above explained procedure, are presented in Fig. 5. The applicability of the subtraction procedure is corroborated by the possibility to smoothly extrapolate these data by appropriate spin-wave models. For ferromagnetic $HoCoC_2$ we apply an extrapolation based on a gaped FM spin-wave dispersion, $\omega = \Delta + D^2k^2$, where Δ is the spin-wave excitation gap and D a spin wave stiffness factor. The resulting inner energy contribution of spin-wave excitations in the low temperature limit is

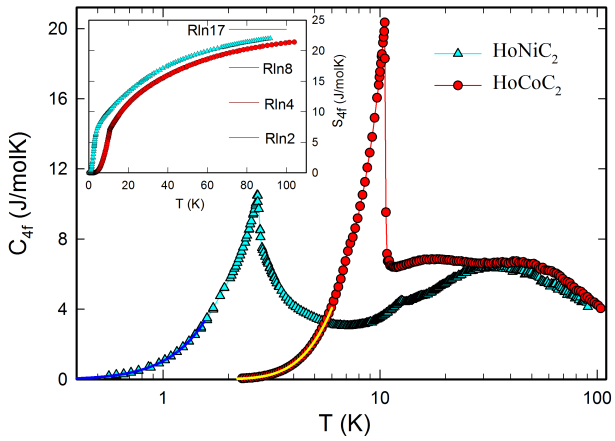

Figure 5: Temperature dependent magnetic specific heat contributions $C_{4f}(T)$ of $HoCoC_2$ and $HoNiC_2$, strong solid, bright yellow and dark blue lines are fits by spin-wave models, Eqn. 2 and 3, respectively (see text); insert: corresponding entropy functions $S_{4f}(T)$ evaluated via Eqn. 4.

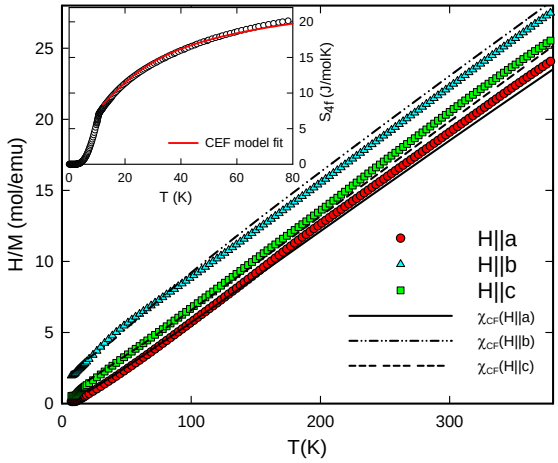

Figure 6: Temperature and field orientation dependent inverse magnetic susceptibility data of $HoCoC_2$ given as symbols and the CEF fit (see text) as lines as labeled; insert: temperature dependent $4f$ magnetic entropy $S_{4f}(T)$ of $HoCoC_2$ given as symbols and the result of the CEF fit as a solid line.

then given by,

$$U_{\mathrm{FMsw}}(T) \propto \int_{\Delta}^{\infty} \frac{\omega\sqrt{\omega-\Delta}}{\mathrm{e}^{\omega/T}-1}\,\mathrm{d}\omega, \qquad (1)$$

where the factor $\sqrt{\omega-\Delta}$ relates to the magnon density of states and for a simple fitting of ω and Δ these parameters are taken in units of Kelvin. The specific heat contribution, $C_{\mathrm{FMsw}}(T)$, is then computed via

$$C_{\mathrm{FMsw}}(T) = \frac{\partial U_{\mathrm{FMsw}}(T)}{\partial T} = \int_{\Delta}^{\infty} \frac{A\left(\frac{\omega}{T}\right)^2 \mathrm{e}^{\omega/T}\sqrt{\omega-\Delta}}{[\mathrm{e}^{\omega/T}-1]^2}\,\mathrm{d}\omega, \qquad (2)$$

where A is a factor $\propto 1/D^3$. The corresponding fit in the temperature range 2.3 – 5 K displayed as bright yellow line in Fig. 5, thus, yields a spin-wave excitation gap, $\Delta = 17.1$ K, which essentially relates to the significant crystal field anisotropy, and factor $A = 0.259\,\mathrm{J/mol\,K^{5/2}}$.

For antiferromagnetic $HoNiC_2$ we apply a relativistic form of the AFM spin-wave dispersion, $\omega = \sqrt{\Delta^2 + D^2k^2}$, as e.g. derived by Batist *et al.* [17]. In this case, the magnon density of states is proportional $\omega\sqrt{\omega^2-\Delta^2}$ and the corresponding specific heat contribution, $C_{\mathrm{AFsw}}(T)$, can be calculated via an expansion of the improper integral yielding a low temperature approximation [18]

$$C_{\mathrm{AFsw}}(T) \simeq A\Delta^{\frac{7}{2}}T^{\frac{1}{2}}e^{-\frac{\Delta}{T}}\left[1+\frac{39}{20}\left(\frac{T}{\Delta}\right)+\frac{51}{32}\left(\frac{T}{\Delta}\right)^2\right]. \qquad (3)$$

The corresponding fit to the magnon specific heat contributions for $T \leq 0.5T_N$ (displayed as dark blue solid line in Fig. 5) via Eqn. (3) yields an estimate for the spin-wave gap $\Delta \simeq 1.26$ K, and a prefactor $A = 0.46\,\mathrm{J/mol\,K^5}$ related to the spin-wave stiffness D. The subtraction of a relatively large nuclear contribution in the relevant temperature interval (compare Fig. 2), of course, introduces some ambiguity for the spin-wave parameters of $HoNiC_2$ while such ambiguities are negligible for $HoCoC_2$.

The temperature dependent $4f$ magnetic entropy gain, $S_{4f}(T)$, of $HoCoC_2$ and $HoNiC_2$ is evaluated by integrating the $4f$ magnetic specific heat contributions displayed Fig. 5 via the basic relation

$$S_{4f}(T) = \int_0^T \frac{C_{4f}}{T'}\,dT', \qquad (4)$$

including the $T \to 0$ extrapolations of $C_{4f}(T)$ by the corresponding spin-wave models (strong solid lines in Fig. 5). The resulting entropy functions are displayed in the insert of Fig. 5. The overall CEF splitting of $HoNiC_2$ is clearly reduced as compared to $HoCoC_2$.

3.5. Crystalline electric field

The above presented magnetic specific heat and entropy functions combined with single crystal susceptibility data of $HoCoC_2$ in section 3.3 and single crystal susceptibility data of $HoNiC_2$ reported by Koshikawa *et al.* [14] provide an experimental basis for analysing CEF effects.

The orthorhombic CEF acting on the 17-fold degenerate, non-Kramers ${}^5I_8$ ground multiplet of the $4f^{10}$ orbital of Ho^{3+} is described by the Hamiltonian [19]

$$\begin{aligned} H_{CF} \;=\; & B_2^0O_2^0 + B_2^2O_2^2 + \\ & B_4^0O_4^0 + B_4^2O_4^2 + B_4^4O_4^4 + \\ & B_6^0O_6^0 + B_6^2O_6^2 + B_6^4O_6^4 + B_6^6O_6^6 \end{aligned} \qquad (5)$$

where B_l^m are the CF parameters and O_l^m are the Stevens operators (for a review, see e.g. Ref. [20]).

Using the software McPhase [21] we performed a simultaneous fit of $C_{4f}(T)$, $S_{4f}(T)$, $1/\chi^{H\|a}(T)$, $1/\chi^{H\|b}(T)$, and $1/\chi^{H\|c}(T)$, for $T > 12$ K in the case of $HoCoC_2$ and $T > 5$ K in the case of

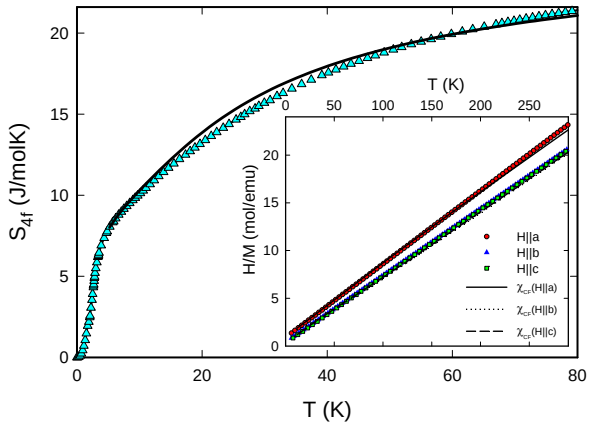

Figure 7: Temperature dependent $4f$ magnetic entropy $S_{4f}(T)$ of $HoNiC_2$ where experimental data are shown as symbols and the fit by the CEF model (see text) as solid line; insert: single crystal inverse magnetic susceptibility data according to Ref. [14] are indicated as symbols and the corresponding CEF fit as lines as labeled.

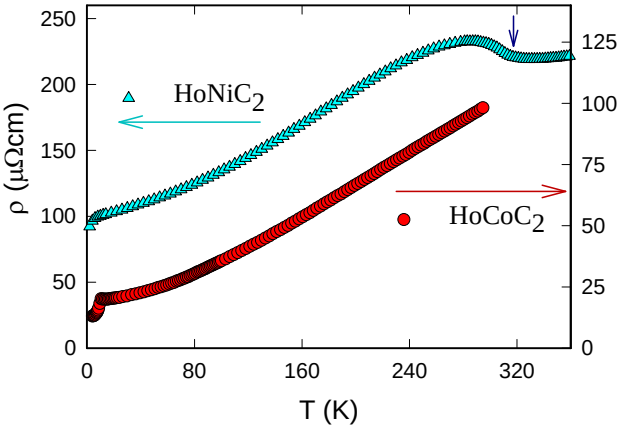

Figure 8: Temperature dependent electrical resistivity, $\rho(T)$, of single crystalline $HoNiC_2$ (scale on right side) and polycrystalline $HoNiC_2$ (scale on left side) with vertical arrow indicating the onset of CDW formation.

$HoNiC_2$, with respect to the nine CEF parameters B_l^m, whereby a simulated annealing algorithm as described in Ref. [22] has been employed. The variation of initial parameter settings and 'annealing conditions' revealed approximately reproducible results for the two lowest order parameters B_2^0 and B_2^2, while seven higher order parameters B_4^0 to B_6^6 remained ambiguous.

The best fit of the experimental susceptibility and entropy data of $HoCoC_2$ is displayed in Fig. 6. An isotropic molecular field, $\lambda = 0.4$ meV and a temperature independent component $\chi_0 = 1.3\times10^{-3}$ emu/mol have been taken into account (compare section 3.2). The resulting relevant crystal field parameters are $B_2^0 \simeq -0.018$ meV and $B_2^2 = -0.099$ meV. The CEF model fit displayed in Fig. 6 suggests a singlet ground state followed by a quasi-doublet $\Delta_{1,2} \simeq 2.5$ meV.

For the fit of $HoNiC_2$ we combined the magnetic entropy results of Fig. 5 with susceptibility data generated from the parameters given in Table 1 of Ref. [14]. The corresponding best fit of the experimental data employing an isotropic antiferromagnetic molecular field, $\lambda = -0.3$ meV, is displayed in Fig. 7 yielding the crystal field parameters $B_2^0 = -0.019$ meV and $B_2^2 = +0.063$ meV. The corresponding level scheme of 17 singlets reveals a singlet ground state followed by lowest levels $\Delta_1 = 0.8$, and $\Delta_2 = 1.7$ meV which contribute to the AFM ordered ground state of $HoNiC_2$ at below 2.8 K. The circumstance that $\Delta_1 > T_N$, may explain the significant reduction of the specific heat anomaly at T_N.

3.6. Charge density wave anomaly in HoNiC$_2$

Temperature dependent electrical resistivity data, $\rho(T)$, of the $HoCo_{1-x}Ni_xC_2$ series reveal a typical metal-like behavior with, of course, a strong increase of the temperature independent residual resistivity due to substitutional disorder in the solid solutions. Most relevant $\rho(T)$ data of $HoCoC_2$ and $HoNiC_2$ are shown in Fig. 8. Among all samples investigated, single crystalline $HoCoC_2$ displays the most distinct magnetic anomaly and the highest room temperature to residual resistivity ratio, $RRR \sim 8$ ($RRR \sim 4$ for polycrystalline $HoCoC_2$) while all other samples of the $HoCo_{1-x}Ni_xC_2$ series exhibit $RRR \leq 2.5$, including $HoNiC_2$ with $RRR \sim 2.3$. The latter, $HoNiC_2$, displays an anomaly at about 317 K (marked by the vertical arrow in Fig. 8), while the corresponding feature further broadens for $HoCo_{0.25}Ni_{0.75}C_2$ (not shown) and cannot be traced for other investigated compositions $HoCo_{1-x}Ni_xC_2$ ($0.5 \leq x \leq 1$). The CDW transition temperature, $T_{CDW} \simeq 317$ K fits well to the extrapolated trend of multiple CDW transitions in the series $RNiC_2$ which were recently re-evaluated for R = Ce – Tb by Shimomura *et al.* [2]. Thereby, multiple CDW transitions observed for R = Gd and Tb appear to merge in one single transition of $HoNiC_2$ visible in Fig. 8. A significant enhancement of the residual resistivity, ρ_0, resulting from CDW instabilities (e.g. compared to $RCoC_2$) is a general feature of the series $RNiC_2$ (R = Ce – Tb) [1] which also applies for $HoNiC_2$.

4. Summary and Conclusions

A continuous solid solution occurs in the pseudo-ternary system $HoCo_{1-x}Ni_xC_2$ ($0 \leq x \leq 1$) adopting the orthorhombic $CeNiC_2$ structure type with non-centrosymmetric space group $Amm2$. The lattice volume increases non-linearly within the solid solution with increasing Ni content. Non-isoelectronic substitution of Co by Ni causes also a deviation of variation of a and b lattice parameters from Vegard's rule and a pronounced increase of the C–C bond number.

Temperature dependent specific heat measurements reveal a non-monotonous variation of the magnetic ordering temperature $T_M(x)$ in the series $HoCo_{1-x}Ni_xC_2$ starting from $HoCoC_2$ with $T_C = 10.6(1)$ K and ending at $HoNiC_2$ with $T_N = 2.78(6)$ K, whereby a minimum of the magnetic ordering temperature is passed at intermediate compositions. The analysis of inverse magnetic susceptibility data in terms of a modified Curie-Weiss model further reveals a sign change of the paramagnetic Curie temperature, which appears to roughly coincide with a minimum of $T_M(x)$.

Using $LuCoC_2$ and $LuNiC_2$ as reference materials for the electron and lattice contributions to the total heat capacities of $HoCoC_2$ and $HoNiC_2$ and employing a simple paramagnetic gas model to evaluate the nuclear contributions, we have extracted the $4f$ magnetic specific heat, $C_{4f}(T)$, and entropy contributions, $S_{4f}(T)$. Thereby, the magnetic specific heat of FM $HoCoC_2$ reveals a significant spin-wave excitation gap, $\Delta \simeq 1.6\,T_C$, which is due to the large single ion anisotropy of this compound. Further combining these thermodynamic data, $C_{4f}(T)$ and $S_{4f}(T)$, with results of single crystal susceptibility measurements on $HoCoC_2$ and with earlier reported single crystal data of $HoNiC_2$ we evaluate estimates of the lowest order CEF parameters $B_2^0 \simeq -0.018$ meV, $B_2^2 = -0.099$ meV and $B_2^0 = -0.019$ meV, $B_2^2 = +0.063$ meV for $HoCoC_2$ and $HoNiC_2$, respectively.

Temperature dependent electrical resistivity data of $HoNiC_2$ display a distinct anomaly at about 317 K which is in line with the trend of CDW transitions earlier reported for the series isostructural compounds $RNiC_2$ (R = Ce – Tb) [1, 2].

References

[1] M. Murase, A. Tobo, H. Onodera, Y. Hirano, T. Hosaka, S. Shimomura, N. Wakabayashi, Lattice constants, electrical resistivity and specific heat of $RNiC_2$, J. Phys. Soc. Japan 73 (10) (2004) 2790–2794. doi:10.1143/JPSJ.73.2790.

[2] S. Shimomura, C. Hayashi, N. Hanasaki, K. Ohnuma, Y. Kobayashi, H. Nakao, M. Mizumaki, H. Onodera, Multiple charge density wave transitions in the antiferromagnets $RNiC_2$ (R = Gd, Tb), Phys. Rev. B 93 (2016) 165108. doi:10.1103/PhysRevB.93.165108.

[3] A. D. Hillier, J. Quintanilla, R. Cywinski, Evidence for time-reversal symmetry breaking in the noncentrosymmetric superconductor $LaNiC_2$, Phys. Rev. Lett. 102 (2009) 117007. doi:10.1103/PhysRevLett.102.117007.

[4] T. Yanagisawa, I. Hase, Nonunitary triplet superconductivity in the noncentrosymmetric rare-earth compound $LaNiC_2$, Journal of the Physical Society of Japan 81 (Suppl.B) (2012) SB039. doi:10.1143/JPSJS.81SB.SB039.

[5] I. O. Bodak, E. P. Marusin, V. A. Bruskov, The crystal structure of $RNiC_2$ compounds (R = Ce, La, Pr), Sov. Phys. Crystallogr. 25 (1980) 355.

[6] W. Jeitschko, M. Gerss, Ternary carbides of the rare earth and iron group metals with $CeCoC_2$- and $CeNiC_2$-type structure, J. Less Common Metals 116 (1986) 147 – 157. doi:10.1016/0022-5088(86)90225-0.

[7] I. O. Bodak, E. P. Marusin, V. A. Bruskov, The crystal structure of compounds RCoC2 (R = Ce, La, Pr), Dokl. Akad. Nauk Ukr. SSR. Ser. A 12 (1979) 1048, in Russian.

[8] W. Schäfer, W. Kockelmann, G. Will, J. K. Yakinthos, P. A. Kotsanidis, Magnetic structures of rare earths R in $RCoC_2$ and $RNiC_2$ compounds, Journal of Alloys and Compounds 250 (1997) 565 – 568. doi:10.1016/S0925-8388(96)02564-9.

[9] W. Schäfer, W. Kockelmann, G. Will, P. Kotsanidis, J. Yakinthos, J. Linhart, Structural and magnetic properties of $RCoC_2$ (R = Pr, Dy, Ho) compounds studied by neutron diffraction, Journal of Magnetism and Magnetic Materials 132 (1994) 243 – 248. doi:10.1016/0304-8853(94)90319-0.

[10] J. Yakinthos, P. Kotsanidis, W. Schäfer, W. Kockelmann, G. Will, W. Reimers, The two-component non-collinear antiferromagnetic structures of $DyNiC_2$ and $HoNiC_2$, Journal of Magnetism and Magnetic Materials 136 (1994) 327 – 334. doi:10.1016/0304-8853(94)00306-8.

[11] H. Michor, V. Levytskyy, F. Schwarzböck, V. Babizhetskyy, B. Kotur, Evolution of magnetic properties in the solid solution $DyCo_{1-x}Ni_xC_2$, Journal of Magnetism and Magnetic Materials 374 (2015) 553 – 558. doi:10.1016/j.jmmm.2014.08.085.

[12] S. Manalo, H. Michor, M. El-Hagary, G. Hilscher, E. Schachinger, Superconducting properties of $Y_xLu_{1-x}Ni_2B_2C$ and $La_3Ni_2B_2N_{3-\delta}$: a comparison between experiment and Eliashberg theory, Phys. Rev. B 63 (2001) 104508. doi:10.1103/PhysRevB.63.104508.

[13] Y. Long, C. Z. Zheng, J. L. Luo, Z. J. Cheng, Y. S. He, Heat capacity of the ternary compounds $ReNiC_2$ (Re= Dy, Ho, Er, and Y), Journal of Applied Physics 89 (2001) 3523–3525. doi:10.1063/1.1333717.

[14] Y. Koshikawa, H. Onodera, M. Kosaka, H. Yamauchi, M. Ohashi, Y. Yamaguchi, Crystalline electric fields and magnetic properties of single-crystalline $RNiC_2$ compounds (R= Ho, Er and Tm), Journal of Magnetism and Magnetic Materials 173 (1997) 72 – 82. doi:10.1016/S0304-8853(97)00177-7.

[15] S. Steiner, H. Michor, B. Hinterleitner, B. Stöger, O. Sologub, E. Bauer, M. Hembara, V. Levytskyy, V. Babizhetskyy, B. Kotur, Structural and electronic properties of $LuCoC_2$ and $LuNiC_2$, Journal of Physics: Condensed Mater, *to be submitted*.

[16] J. E. Gordon, C. W. Dempesy, T. Soller, Nuclear specific heat of holmium, Phys. Rev. 124 (1961) 724–725. doi:10.1103/PhysRev.124.724.

[17] R. De Batist, R. Gevers, M. Verschueren, Magnon contribution to the low-temperature specific heat of UO_2, physica status solidi (b) 19 (1967) 77–88. doi:10.1002/pssb.19670190108.

[18] M. A. Continentino, S. N. de Medeiros, M. T. D. Orlando, M. B. Fontes, E. M. Baggio-Saitovitch, Anisotropic quantum critical behavior in $CeCoGe_{3-x}Si_x$, Phys. Rev. B 64 (2001) 012404. doi:10.1103/PhysRevB.64.012404.

[19] M. Hutchings, Point-charge calculations of energy levels of magnetic ions in crystalline electric fields, Vol. 16 of Solid State Physics, Academic Press, 1964, pp. 227 – 273. doi:10.1016/S0081-1947(08)60517-2.

[20] E. Bauer, M. Rotter, Chapter 5: Magnetism of complex metallic alloys: Crystalline electric field effects, in: E. Belin-Ferre (Ed.), Euro-school on materials science; Properties and applications of complex intermetallics, Vol. 2 of Book Series on Complex Metallic Alloys, World Scientific, Singapore, London, 2010, pp. 183 – 248.

[21] M. Rotter, Using mcphase to calculate magnetic phase diagrams of rare earth compounds, Journal of Magnetism and Magnetic Materials 272–276, Supplement (2004) e481 – e482, proceedings of the International Conference on Magnetism (ICM 2003). doi:10.1016/j.jmmm.2003.12.1394.

[22] S. Kirkpatrick, C. Gelatt Jr., M. Vecchi, Optimization by simulated annealing, Science 220 (1983) 671 – 680. doi:10.1126/science.220.4598.671.